

# Coupled weather research and forecasting–stochastic time-inverted lagrangian transport (WRF–STILT) model

Thomas Nehr Korn · Janusz Eluszkiewicz ·  
Steven C. Wofsy · John C. Lin · Christoph Gerbig ·  
Marcos Longo · Saulo Freitas

Received: 9 June 2009 / Accepted: 21 April 2010 / Published online: 5 May 2010  
© Springer-Verlag 2010

**Abstract** This paper describes the coupling between a mesoscale numerical weather prediction model, the Weather Research and Forecasting (WRF) model, and a Lagrangian Particle Dispersion Model, the Stochastic Time-Inverted Lagrangian Transport (STILT) model. The primary motivation for developing this coupled model has been to reduce transport errors in continental-scale top-down estimates of terrestrial greenhouse gas fluxes. Examples of the model's application are shown here for backward trajectory computations originating at CO<sub>2</sub> measurement sites in North America. Owing to its unique features, including meteorological realism and large support base, good mass conservation properties, and a realistic treatment of convection within STILT, the WRF–STILT model offers an attractive tool for a wide range of applications, including inverse flux estimates, flight planning, satellite validation, emergency response and source attribution, air quality, and planetary exploration.

## 1 Introduction

The work of Uliasz (1993) demonstrated that coupling a Lagrangian Particle Dispersion Model (LPDM) to a numerical weather prediction (NWP) model offers the best tool for realistic atmospheric transport simulations on regional, continental and, under some circumstances, global scales. The use of Lagrangian Particle Dispersion Models (LPDMs) can be traced back to earlier examples, such as Yamada and Bunker (1988) and Pielke et al. (1983). A review of the mathematical and physical foundations of stochastic turbulence modeling can be found in Rodean (1996). The Lagrangian approach, both in the forward and backward (receptor-oriented) mode (Seibert and Frank 2004), is the method of choice when dealing with highly localized sources or receptors, while NWP models offer the most realistic wind fields with which to drive the LPDM. Current applications include air quality (Draxler and Hess 1997), emergency response and source attribution (Buckley 2000; Seibert and Frank 2004), surface flux estimates (Flesch et al. 1995; Gerbig et al. 2003), validation and analysis of satellite data (Worden et al. 2007; Avey et al. 2007), and flight planning (Forster et al. 2004; Lin et al. 2007). Future applications may include biogenic source attribution on Mars, envisioned as motivation for the spacecraft missions planned for the next decade (Calvin et al. 2007).

In view of the recognized potential of coupled LPDM/NWP models and prompted by the Chernobyl disaster, several such models have been developed and are currently supported and extensively used. The availability of multiple models is highly beneficial, as a model-ensemble approach is a very promising way of reducing transport uncertainties in dispersion modeling (e.g., Galmarini et al. 2004). Of particular note are the Colorado State University

---

T. Nehr Korn (✉) · J. Eluszkiewicz  
Atmospheric and Environmental Research, Inc.,  
Lexington, MA, USA  
e-mail: tnehrkor@aer.com  
URL: <http://www.aer.com>

S. C. Wofsy · M. Longo  
Harvard University, Cambridge, MA, USA

J. C. Lin  
University of Waterloo, Waterloo, ON, Canada

C. Gerbig  
Max-Planck-Institut für Biogeochemie, Jena, Germany

S. Freitas  
Center for Weather Forecasts and Climate Studies (CPTEC),  
INPE, Cachoeira Paulista, Brazil

LPDM coupled to the Regional Atmospheric Modeling System (RAMS) model (Uliasz 1993; Cotton et al. 2003; Pielke et al. 1992; Buckley 2000) and the FLEXPART model coupled to the European Centre for Medium-Range Weather Forecast (ECMWF) and the Weather Research and Forecasting (WRF) models (Stohl et al. 2005). A third coupled LPDM/NWP model, the Stochastic Time-Inverted Lagrangian Transport (STILT) model coupled to the WRF model, forms the focus of this paper. The STILT model was originally developed for carbon science applications, but it should be attractive to a wide range of research and operational applications. Given its large existing and potential user base, we believe that a documentation of the coupled WRF–STILT model, highlighting its unique aspects, will be helpful to the community. With this in mind, in this paper we will describe the numerical aspects of the coupling between the STILT and WRF models and present some general results demonstrating the performance of the coupled model, particularly with regard to mass conservation. Given that the WRF model is used extensively in both operational and research settings in the US and worldwide, this large support and user base assures that the coupled WRF–STILT model will “grow” with new advances in the LPDM and NWP fields.

## 2 WRF–STILT coupling

The STILT model, based on the HYSPLIT model developed at NOAA’s Air Resources Laboratory (Draxler and Hess 1997, 1998), is described in Lin et al. (2003), while the WRF model is described in Skamarock and Klemp (2008) and extensively documented in Skamarock et al. (2005). Consequently, in this section, we confine ourselves to describing those aspects of both models that are directly relevant to the coupling between them. This coupling utilizes concepts and approaches developed for the coupling between the STILT model and another widely used mesoscale model, the RAMS model in its Brazil implementation BRAMS (Brazilian RAMS) (Freitas et al. 2005, 2009; Medvigy et al. 2005). Recently, STILT has been coupled to ECMWF forecasts (Gerbig et al. 2008). Besides WRF, RAMS, and ECMWF, the STILT model is currently configured to be driven by meteorological fields produced by the National Centers for Environmental Prediction (NCEP) global and regional data assimilation systems. The ability of utilizing fields produced by different meteorological drivers allows for in-depth model intercomparison studies. The results presented in this paper have been obtained using version 2.1.2 of the Eulerian mass-coordinate dynamical core of WRF, which is part of the Advanced Research WRF supported by the National Center for Atmospheric Research (NCAR). As this version does not support nudging, we

employed a series of overlapping 30-h runs to produce continuous simulations for months at a time (see Sect. 3.1). More recent applications (see Sect. 4) have used version 2.2 (which includes nudging capabilities) and version 3.0.

### 2.1 STILT model grids

To minimize errors resulting from horizontal interpolation of model variables, the STILT model is designed to perform all computation on the horizontal grid of the meteorological input dataset. (Particles that reach the edge of the model grid are terminated; in applications using nested grids, computations are restarted using meteorological fields from outer nests.) Currently supported map projections are conformal, including polar stereographic, Mercator, and Lambert (the latter has been used in the work described herein). By default, the code assumes that all model variables are located at the same mesh points, i.e., that there is no staggering of mass and momentum variables in the horizontal. Input datasets from models using staggered grids must thus be either interpolated to an unstaggered grid or special handling must be implemented within the STILT code whenever staggered variables (usually the horizontal wind components) are interpolated to trajectory locations. The latter approach is taken in STILT for the BRAMS and WRF model input.

The STILT/HYSPLIT models use a  $\sigma$ – $z$  vertical coordinate, defined as

$$\sigma = \frac{z_{\text{top}} - z_{\text{msl}}}{z_{\text{top}} - z_{\text{gl}}} \quad (1)$$

where  $z_{\text{top}}$  is the model top height,  $z_{\text{msl}}$  is the height of the model level (above mean sea level, MSL), and  $z_{\text{gl}}$  is the height of the model terrain (above MSL). In the default mode, the STILT model uses a set of vertical coordinate values in which the grid level index  $k$  and model level height above ground for a gridpoint at MSL are related through a quadratic relationship (Draxler and Hess 1997)

$$h \equiv z_{\text{msl}} - z_{\text{gl}} = ak^2 + bk + c \quad (2)$$

with  $a = 30$  m,  $b = -25$  m, and  $c = 5$  m and  $z_{\text{top}} = 25$  km. The default mode is employed when STILT is driven by pressure-level analyses, e.g., outside of the domain covered by WRF or another mesoscale model. For runs driven by WRF or ECMWF winds, the values of  $h$  are specified in a separate file, while for NWP models employing the  $\sigma$ – $z$  vertical coordinate, such as RAMS, their model levels are used directly in STILT.

### 2.2 STILT input variables

The most important meteorological variables required for trajectory calculations in STILT are vertical profiles of the

horizontal and vertical wind components. The horizontal winds (in  $\text{m s}^{-1}$ ) are converted internally to grid lengths/min, whereas the vertical velocity is converted from the meteorological input to its internal representation of  $d\sigma/dt$ . In addition, profiles of temperature, pressure, and humidity are needed and converted internally to pressure, virtual potential temperature, relative humidity, and air density. Variables at the surface needed for the computation of sigma-level profiles are the terrain height, pressure, and temperature.

Additional two-dimensional fields are used for the determination of turbulence parameters (such as surface roughness length; latent and sensible heat flux at the surface; friction velocity). The height of the planetary boundary layer can be either computed internally in STILT, or provided as an input from the meteorological model. Other two-dimensional fields (such as radiative fluxes at the surface) are used in coupling the STILT output to biosphere models (e.g., for carbon cycle applications). Coupling of the parameterization of deep moist convection within RAMS or WRF with the convective flux parameterization within STILT requires additional variables, as described in Sect. 2.7.

### 2.3 WRF model grids

The computational grid of the WRF model is regularly spaced in one of several possible map projections, including the STILT-supported conformal projections (polar stereographic, Mercator, and Lambert). A global latitude–longitude grid option is also available starting with version 3.0. These grids may be nested, but each nest is output separately and treated as a separate grid in STILT. The vertical coordinate used by the WRF model is a terrain-following pressure–sigma coordinate system based on the dry hydrostatic pressure  $p_{dh}$ . It is defined as

$$\eta = \frac{p_{dh} - p_{dht}}{\mu_d}, \text{ where } \mu_d \equiv p_{dhs} - p_{dht}. \tag{3}$$

Here  $p_{dhs}$  and  $p_{dht}$  are the dry hydrostatic pressure at the surface and the model top, respectively. Note that the symbol  $\eta$  has been adopted by the WRF developers for this coordinate system, although it is different from the traditional  $\eta$  coordinate (UCAR 2000).

### 2.4 WRF wind and thermodynamic variables

The standard output provided by the WRF model includes instantaneous values of the grid-relative horizontal wind components ( $u, v$ ) and the geometric vertical velocity  $dz/dt$  (all three components in  $\text{m s}^{-1}$ ) at the staggered grid locations of the Arakawa C-grid (Arakawa and Lamb 1977). The WRF–STILT interface provides the option to

use these velocities, in which case only minor changes are required to the WRF model code.

The WRF model equations are formulated as perturbation equations with respect to a dry hydrostatic reference state at rest. Thermodynamic quantities available in the standard WRF model output include the (full or perturbation) potential temperature, the base state and perturbation pressure, and the water vapor mixing ratio. Additional WRF model variables are required by the WRF–STILT interface to permit computation of the WRF model level heights (see Sect. 2.1). They include the dry inverse density  $\alpha_d$ , needed for the integration of the WRF hydrostatic equation

$$\frac{\partial \Phi}{\partial \eta} = -\alpha_d \mu_d \tag{4}$$

and the base state and perturbation values of  $\mu_d$ .

### 2.5 WRF mass-coupled wind variables

Aside from the accuracy of the meteorological fields, an important requirement for the meteorological input fields for an LPDM is that they conserve mass (Lin et al. 2003). While the WRF and other NWP models usually conserve mass internally to a high degree, this can no longer be guaranteed if the model variables are transformed and temporally and spatially interpolated (by the NWP model’s postprocessing and/or the LPDM’s preprocessing routines). To minimize these problems, the WRF–STILT interface provides the option to make use of time-averaged values of the mass-coupled velocities used internally by WRF for the advection of passive scalars. The mass-coupled horizontal velocities ( $U, V$ ) are defined as

$$U = u\mu_d/m, V = v\mu_d/m \tag{5}$$

where ( $u, v$ ) are the grid-relative wind components, and  $m$  is the map scale factor. A coupled vertical velocity is similarly defined as

$$\Omega = (\mu_d/m) \frac{d\eta}{dt}. \tag{6}$$

The time stepping used in the WRF model for the slow (non-acoustic) modes is a third-order Runge–Kutta scheme. Acoustic tendencies (terms of the compressible governing equations that admit sound waves) are stepped on a shorter time step, using deviations from the last large time step values of the Runge–Kutta scheme. Passive scalars are advected using values of  $U, V$ , and  $\Omega$  that are time-averaged over the acoustic steps. For use by the STILT model,  $U, V$ , and  $\Omega$  are further averaged over all large time steps within the output interval of the WRF model (this is a user-specified parameter; experiments reported here used an interval of 1 h). These time-averaged

mass-coupled winds ( $U$ ,  $V$ , and  $\Omega$ ), along with the convective fluxes discussed in Sect. 2.7, are the only fields averaged in time between output times; all other fields, including the un-coupled wind components ( $u$ ,  $v$ ,  $w$ ), are output as instantaneous values.

## 2.6 Vertical interpolation and variable transformation

In order to utilize WRF fields, the STILT source code primarily required modifications in its meteorological input module and in the interpolation of the input profiles to the STILT model levels. Additional changes, which are not described in detail here, were required throughout a number of modules to account for the horizontal and vertical staggering of the wind components, and the treatment of time-averaged rather than instantaneous model values. Both of these aspects are quite similar to the provisions for the RAMS model input.

The meteorological input module was modified to process the required and optional WRF model fields. Base state and perturbation quantities of pressure and  $\mu_d$  are combined to full values in this module. In order to perform the vertical interpolation from WRF to STILT model levels, the height above terrain of the STILT  $k$ th model level is first computed using Eq. 1.

$$h_k \equiv z_{\text{msl},k} - z_{\text{gl}} = (1 - \sigma_k)(z_{\text{top}} - z_{\text{gl}}) \quad (7)$$

The corresponding height above ground for the input WRF mass model levels is obtained by upward integration of Eq. 4

$$\Delta z_k = h_k - h_{k-1} = -\frac{1}{g} \mu_d \bar{\alpha}_d \Delta \eta_k \quad (8)$$

where  $\Delta \eta_k$  is the spacing of the WRF mass levels, and  $\bar{\alpha}_d$  is the layer-average value of  $\alpha_d$ , computed from the mass level values as in Skamarock et al. (2005, Eq. 3.28). The WRF mass level model variables are then interpolated linearly in height from the WRF mass levels to the STILT model levels. The vertical interpolations are a potential source of error and non-conservation of mass; however, sensitivity tests using choices of STILT levels that either minimized or maximized the amount of interpolation from WRF to STILT levels showed that there was little impact on either computed trajectories or mass conservation diagnostics.

## 2.7 Accounting for convection in STILT

The effects of moist convection need to be parameterized in NWP model simulations that use horizontal grid spacings that do not permit a realistic explicit simulation of convective motions (typically resolutions of 10 km or coarser require parameterizations, and resolutions of 2 km

or less are required for realistic explicit simulations of convection). Modern LPDMs account for the impact of parameterized moist convective motions on particle dispersion (e.g., Forster et al. 2007). (The effects of dry convective overturning are treated separately by the stochastic velocity components derived from boundary layer turbulence parameters.) In its original implementation, the STILT model either ignored the impact of moist convective motions on the trajectory calculations or treated them in a simplistic way to create an upper bound by vertically mixing all cells with positive convective available potential energy (CAPE) up throughout the entire unstable layer (defined by the limit of convection) (Gerbig et al. 2003). The availability in both the RAMS and WRF models of moist convective mass fluxes, parameterized using the Grell et al. (1994) or Grell and Devenyi (2002) schemes, allows for a more sophisticated approach, in which the STILT model takes detailed account of moist convective mass fluxes in the dispersion of particles, incorporating the vertical profiles of up- and downdrafts, and detrainment and entrainment fluxes between the environment and convective elements. This scheme, originally for the STILT/BRAMS coupling, extends the method described by Freitas et al. (2000). A distinguishing aspect of this scheme is that it directly uses the moist convective mass fluxes generated by the NWP model in a stochastic fashion (particle has a higher probability by a specific mass flux, with probability in direct proportion to the magnitude of the mass flux), and the WRF and BRAMS models have been modified to output them in a format compatible with STILT.

### 2.7.1 Convective fluxes in WRF

In the WRF model, the Grell–Devenyi scheme (Grell and Devenyi 2002) at the time was implemented for deep moist convection only (shallow, non-precipitating convection was not yet implemented). The scheme uses a 144-member ensemble of parameterizations, allowing for 3 different values of precipitation efficiency, 3 different values for a numerical parameter related to the cloud base mass flux normalization, and 16 different closure assumptions. Within the scheme, all computed convective fluxes are normalized by the cloud base mass flux. The normalized fluxes are averaged over the ensemble members, and then scaled by the ensemble-averaged cloud base mass flux.

The Grell–Devenyi scheme is a mass flux scheme, in which the grid-cell average of the updraft mass flux profile is given by

$$m_u(z, \lambda) = m_b(\lambda) \eta_u(z, \lambda) \quad (9)$$

where  $\lambda$  denotes the ensemble member,  $m_b$  is the mass flux at cloud base, and  $\eta_u$  is the normalized updraft mass flux profile. Similarly, the downdraft mass flux is given by

$$m_d(z, \lambda) = m_o(\lambda)\eta_d(z, \lambda) \quad (10)$$

where  $m_o$  is the mass flux at the originating level of the downdraft.  $m_o$  is related to the cloud base mass flux  $m_b$  through a parameter  $\varepsilon$  that depends on the precipitation efficiency  $(1 - \beta)$ , the total condensation in the updraft  $I_1$ , and the evaporation in the downdraft  $I_2$  (Grell 1993, Eq. A.24)

$$m_o(\lambda) = \varepsilon(\lambda)m_b(\lambda) = \frac{\beta(\lambda)I_1(\lambda)m_b(\lambda)}{I_2(\lambda)} \quad (11)$$

The vertical profiles of the normalized up- and downdraft mass fluxes are controlled by the fractional entrainment and detrainment rates, which are then used to arrive at the final values of entrainment and detrainment rates based on additional assumptions about entrainment and detrainment at the top and bottom of the up- and downdrafts. The entrainment and detrainment mass fluxes are used for the computation of convectively induced tendencies of the environment. Details of this computation, and the mass budget of the convective fluxes, are shown in Grell (1993, Fig. B1). An internal consistency check for mass conservation is included in the scheme.

### 2.7.2 Convective fluxes within STILT

For the Grell-type convection schemes, STILT uses vertical profiles of the mass flux within the updrafts and downdrafts, and the entrainment of mass from the environment into the up- and downdrafts (and detrainment into the environment from the up- and downdrafts). The up- and downdraft mass fluxes (in  $\text{kg m}^{-2} \text{s}^{-1}$ ) are given at the staggered model levels, while the entrainment and detrainment fluxes (also in  $\text{kg m}^{-2} \text{s}^{-1}$ ) are defined at mass levels, representing the change in up- or downdraft mass flux over the layer depth due to entrainment and detrainment. The grid-cell averages of up- and downdraft mass fluxes at cloud base are converted to a fractional coverage, using the square root of TKE as updraft velocity (with the PBL scheme used in the experiments reported here, TKE is not available from the WRF output, and an assumed value of  $1 \text{ m s}^{-1}$  is used instead). Vertical profiles of up- and downdraft vertical velocity are then derived from the flux profiles and the (vertically constant) fractional coverage of the up- and downdrafts. The vertical profiles of the up- and downdraft mass fluxes, and their changes due to entrainment and detrainment, are used to compute the probability of individual particles being located within the environment or in an up- or downdraft.

Rigorous tests to ensure adherence to the well-mixed criterion were conducted during the development and implementation of the convective scheme in STILT. The well-mixed criterion is a physical principle that states

particles in a LPDM should maintain a well-mixed distribution that follows the profile of atmospheric density, a direct consequence of the second law of thermodynamics (Thomson 1987). Tests involved large ensembles of 10,000 particles, initially well mixed in the vertical, with their convective motion integrated over long times (up to several weeks) in real convective cases to ensure well-mixedness within the column.

To support the use of WRF-generated convective mass fluxes, changes were needed in the computation of the vertical levels passed to the Grell convection subroutine in STILT, since the existing RAMS implementation assumed that the fluxes were available at the staggered vertical grid of the RAMS model data. In addition, the vertical interpolation routine for WRF input data had to be augmented to support a remapping of the mass fluxes to the STILT model levels. As was the case for the vertical velocity, the wind-level up- and downdraft mass fluxes are interpolated to the staggered STILT levels, while the entrainment and detrainment fluxes are redistributed to the STILT layers.

## 3 Sample results

The WRF–STILT interface has been extensively used during  $\text{CO}_2$  simulations over the Northeastern United States. The experimental setup for these simulations is described in the next section, followed by a discussion of selected results that illustrate general aspects of the WRF–STILT model, including mass conservation and sensitivity to model resolution and the treatment of convection. Additional applications are discussed in Sect. 4.

### 3.1 Experimental setup

The results presented in this paper were obtained using version 2.1.2 of the Advanced Research WRF (ARW) (Skamarock et al. 2005), with the following physics options:

- Radiation: RRTM scheme (Mlawer et al. 1997) for the longwave and Goddard scheme (Chou and Suarez 1994) for the shortwave.
- Planetary Boundary Layer: Yonsei University (YSU) scheme coupled with the NOAH land surface model and the MM5 similarity theory based surface layer scheme.
- Microphysics: Purdue Lin scheme (Lin et al. 1983; Chen and Sun 2002).
- Convection: Grell–Devenyi ensemble mass flux scheme (Grell and Devenyi 2002).

The selected radiation schemes are generally considered the most accurate choices available in version 2 of WRF.

The YSU PBL scheme was found by Fast (2005) to perform better in estimating the height of the PBL than higher moment schemes. The choice of the microphysics scheme is consistent with that of Fast (2005), while the choice of the cumulus convection scheme enabled us to include the computed convective mass fluxes in the meteorological input fields for STILT, as described in Sect. 2.7.

The outer model domain with a grid resolution of 40 km was chosen to cover most of the continental North America using a Lambert conformal projection (see Fig. 1). In addition, a nested domain with 8-km grid resolution was placed over the NOAA Earth System Research Tall Tower CO<sub>2</sub> monitoring station near Argyle, Maine (45.03°N, 68.68°W), using one-way nesting. All runs described here used 30 levels. For these simulations, the Grell–Devenyi scheme was used at both the 40 and 8 km resolutions. At 8 km, the resolution is near the limit of applicability for convective parameterizations, but still above the resolution where moist convection can be simulated explicitly. Model results were output hourly. North American Regional Reanalysis fields (NARR, Mesinger et al. 2006) were used for initial and lateral boundary condition data. The NARR fields are generated using the NCEP regional data analysis system (EDAS), and are available on a 32-km Lambert conformal grid. A series of free-running forecasts were used to generate continuous meteorological fields for May through September of 2004. Each forecast was started at 00 UTC, and hours 6–30 of the forecast were used (thus avoiding spin-up artifacts and other transients during the first 6 h).

### 3.2 Verification of meteorological fields

For a statistical evaluation, we compute verification statistics both against radiosonde observations and gridded analysis fields. The set of radiosonde observations used in this analysis is shown in Fig. 2. The comparison against the radiosondes uses the STILT trajectory model: for each station location, observation level, and time, the trajectory

**Fig. 1** WRF domains. Shown in red are the locations of two measurement sites: the Argyle tower in Maine and the WLEF tower in Park Falls, Wisconsin

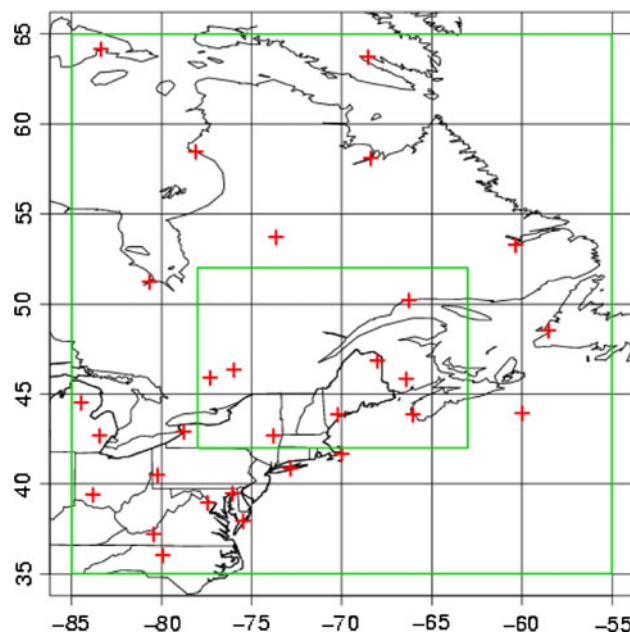
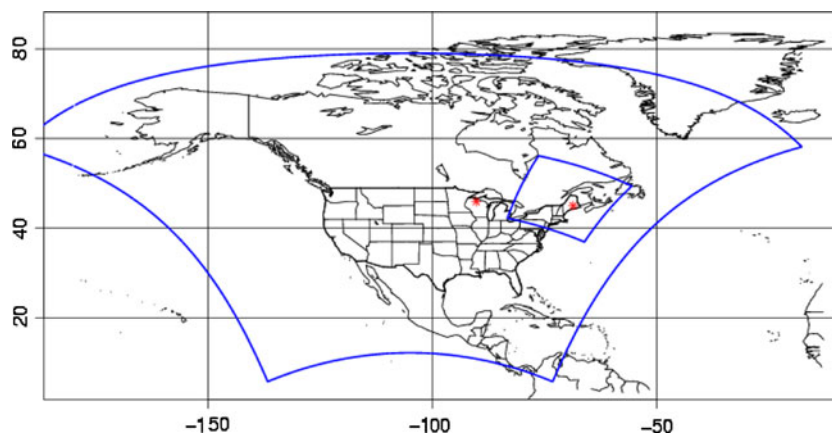


**Fig. 2** Radiosonde locations used in the verification statistics. Green outlines denote longitude–latitude limits for grid points used in the gridded verification statistics, referred to as the Northeast US (outer green box) and inner domain (inner green box)

model is run for a brief integration time, and the corresponding zonal and meridional displacements are then compared against the observed zonal and meridional winds. This approach, while computationally slow, has the advantage that it directly uses the ARL-formatted input meteorological files used by STILT, and can thus be directly applied to any of the various meteorological inputs compatible with STILT, regardless of what grid structure or model variables are used. It also provides a test of the way the meteorological information is actually used in the trajectory model.

A comparison of the WRF fields against gridded analysis allows a more detailed examination of the evolution of the forecast error with lead-time, and of its dependence on vertical level. For a densely sampled region like the North

American continent, radiosonde observations still constitute the most important data source for the analysis, although other observations and information propagated by the forecast model may lead to non-trivial differences. For the area of the Northeast US bounded by the outer green box in Fig. 2, error statistics were accumulated for all NARR analysis grid points contained within this box. The gridpoint statistics used (instantaneous, not time-averaged) WRF model results interpolated in space to the analysis grid points.

Sample statistics obtained using both methods (using all the stations and grid points within the outer green box in Fig. 2) are shown in Fig. 3 for a total of 32 forecasts between 1 June and 10 July 2004. Results are shown separately for forecast valid times at 12 UTC (this corresponds to a 12-h forecast for the WRF fields) and 00 UTC

(corresponding to a 24-h WRF forecast). As expected, the WRF errors are larger at the 24-h forecast lead-time than at 12 h. The gridded error statistics show generally smaller error magnitudes than those based on radiosondes, but they show the same qualitative dependence on level and forecast lead-time. It is unclear whether the differences are due to the differences in the verification procedure, the fact that the verifying analyses are also used as initial and boundary conditions for the WRF forecast (however, given the size of the outer WRF domain, the influence of the lateral boundary conditions is not likely a major factor at 12 and 24 h into the forecast), or simply the result of sampling differences.

A more complete picture of the forecast error growth over the entire 30-h forecast length is shown in Fig. 4. Lin et al. (2007) found qualitatively similar error growth of

**Fig. 3** Verification statistics for WRF forecasts valid at 12 UTC (left panel) and 24 UTC (right panel, note change in scale). Shown are errors for the Northeast US based on radiosonde (circles) and NARR analysis (triangles) comparisons, for the u- (solid lines) and v-wind (dashed lines) components

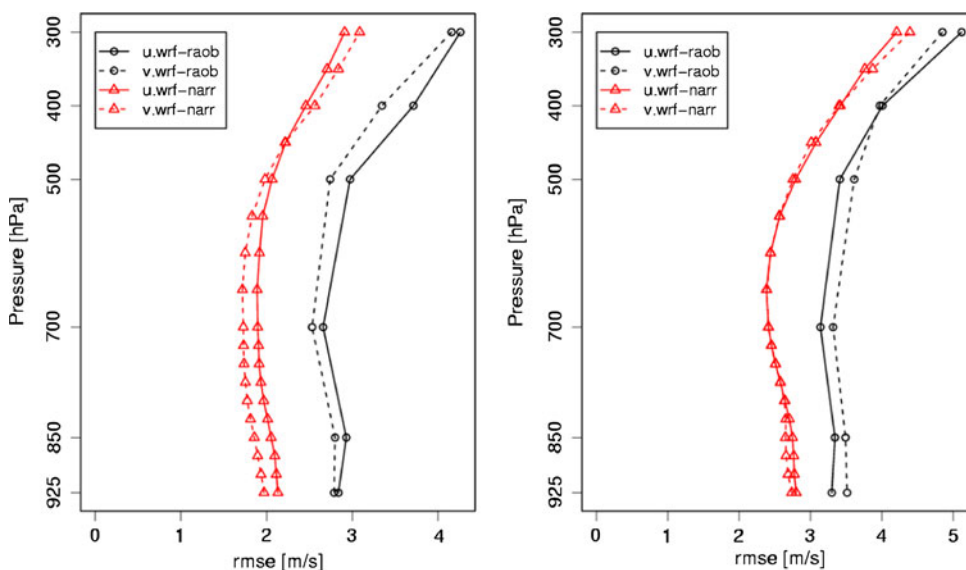
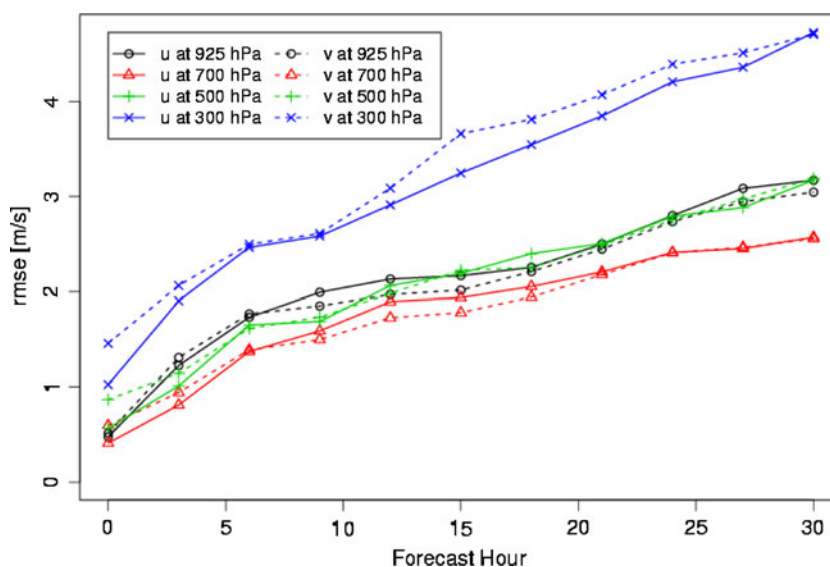


**Fig. 4** Evolution of RMS forecast errors with respect to NARR analyses over the Northeast US. Errors are shown for the u- (solid lines) and v-wind components (dashed lines), at pressure levels 925 hPa (circles), 700 hPa (triangles), 500 hPa (cross), and 300 hPa (multisymbol)



forecast winds compared to radiosonde observations for mesoscale models during May/June 2003 (because of differences in averaging, results are not directly comparable). In more recent work (see Sect. 4), nudging of the forecast to gridded analyses was used to limit this error growth.

Radiosonde verification statistics were also computed for the WRF fields from the inner domain, for the same dates and times as shown in Fig. 3 (gridded verification statistics were not computed for the inner domain, since the verifying analysis is only available at a coarser resolution). The results are shown in Fig. 5. For comparison, the error statistics for the coarse-resolution WRF forecasts, computed for the same times and radiosondes, are also shown in Fig. 5. There is no clear benefit of using higher horizontal resolution in terms of these statistics, with smaller errors at some levels (400 and 300 hPa), and larger errors at others (850 hPa). However, there are cases where using nested fields has a large effect on simulated trajectories, as is shown in the next section.

**Fig. 5** As Fig. 4, except for radiosonde locations over the inner domain box in Fig. 2, for coarse resolution (*circles* 40-km grid spacing) and high-resolution (*triangles* 8-km grid spacing) WRF fields, for 20 days in June 2004

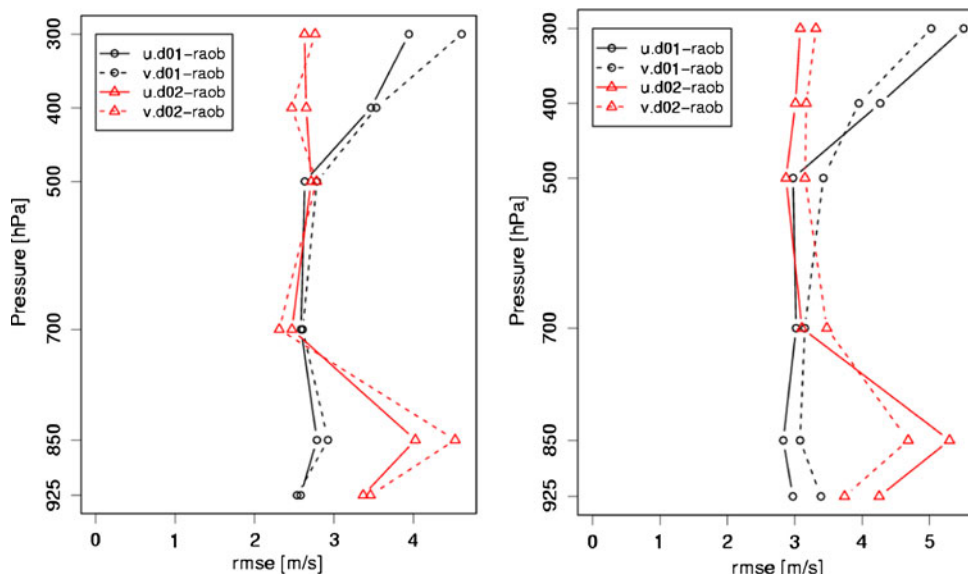
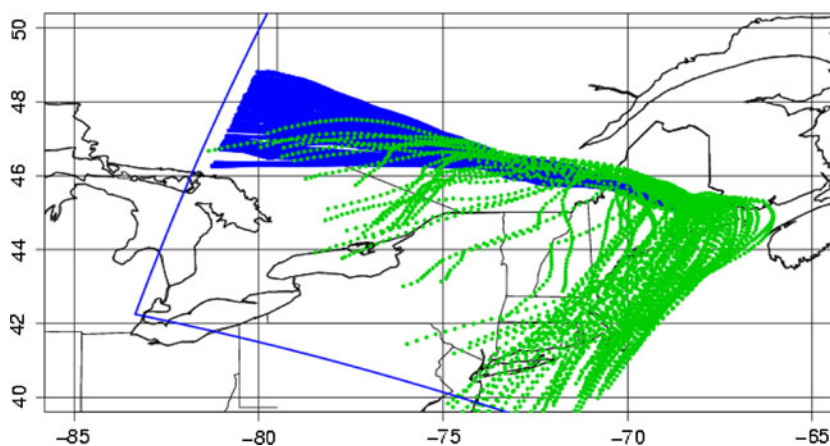


**Fig. 6** Particle locations for 30-h back trajectories from Argyle, 23 UTC 23 June 2004, using coarse resolution (*green*) and nested (*blue*) WRF model fields. The nested domain boundary is shown as a *blue line*



Another aspect of the meteorological simulation with a large effect on the realism of dispersion computations is the representation of the turbulent mixing in the planetary boundary layer (PBL), particularly the PBL height. Error statistics similar to those for the radiosonde winds can be computed for PBL heights. However, estimates of PBL heights from radiosondes are limited by the insufficient temporal sampling, and more accurate and frequent estimates from alternative observing platforms (e.g., boundary layer profilers) are limited to special field experiments.

### 3.3 Trajectory results

One of the motivations for using the WRF model fields was that it is possible to include nested domains with increased resolution near the receptor site (back trajectories shown here were computed for the 107 m AGL level of the Argyle tower), where the details of the smaller-scale circulations can play an important role in the simulated trajectories. The

effect of using nested versus coarse-resolution input fields on the resulting trajectories is particularly dramatic for the case shown in Fig. 6 (back trajectories starting at 23 UTC on 23 June 2004). A substantial number of trajectories computed using coarse-resolution fields approach the Argyle tower from the South and Southeast, abutting the coastline, whereas the higher resolution fields result in trajectories that approach straight from the West. The synoptic situation for this case is characterized by a weak surface low with a trough line extending northward into Maine. There are important differences in how this feature is resolved in the coarse and nested WRF model output fields, which results in low-level flow from the North at Argyle in the nested WRF output, and a flow more from the East in the coarse-resolution WRF fields. An additional factor causing differences in the trajectories is that the nested WRF fields have much stronger vertical velocities (not shown here), resulting in a much larger proportion of particles at higher levels in the nested run, where winds are predominantly from the west.

The effects of including the convective mass fluxes in the trajectory calculations are generally small for the mid-latitude surface locations we have examined. A case that did show some sensitivity was for a receptor at the Argyle location on 18 UTC 16 July 2004. Figure 7 shows results for the 30-h back trajectories in this case. As is evident from the top left panel, the vertical distribution of the particles from trajectory computations with and without convective mass fluxes begin to diverge after 18 h, i.e., at 00 UTC. An examination of the 6-h period between 24 and 30 h backward trajectory time (12–18 UTC on 15 July) shows the particles in an area of convective activity predicted by the WRF model. The spatial distribution and magnitude of the WRF-predicted convective precipitation agrees well with the corresponding Stage IV precipitation analysis in this case. Stage IV precipitation analyses, which are produced operationally by River Forecast Centers and mosaiced into a national 4-km resolution grid by the National Centers for Environmental Prediction (NCEP), are based on multi-sensor precipitation analyses combining

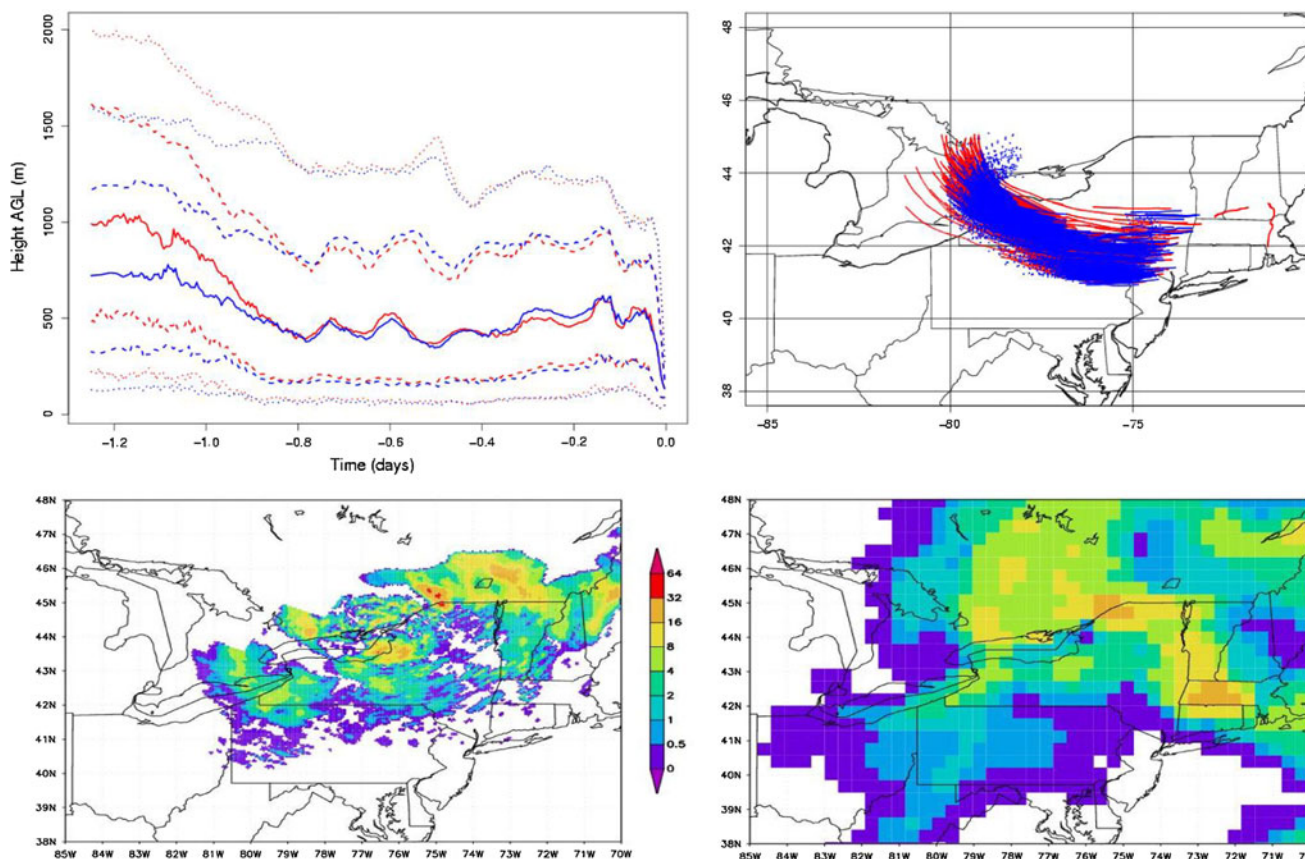


**Fig. 7** Effect of convective precipitation on computed trajectories. *Top left* time series of 10th and 90th (dotted), 25th and 75th (dashed), and 50th (solid) percentiles of height above ground for the particles along back trajectories beginning at 18 UTC 16 July 2004, shown in red for the case with convection, and in blue for the case without convection. *Top right* particles locations between 24 and 30 h back

trajectory time, shown in red for the convective case, and overplotted in blue for the case without convection. *Bottom left* stage IV observed precipitation ( $\text{kg}/\text{m}^2$ ) between 12 and 18 UTC 15 July 2004. *Bottom right* WRF-predicted convective precipitation ( $\text{kg}/\text{m}^2$ ) between 12 and 18 UTC 15 July 2004

radar precipitation estimates, raingauge data, and manual quality control (additional information is available at <http://www.emc.ncep.noaa.gov/mmb/ylin/pcpanl/>).

The impact on the trajectory locations is too small to be readily apparent in the plot of particle positions shown in Fig. 7. A more relevant measure related to the sensitivity of simulated  $\text{CO}_2$  concentration on surface fluxes is the “footprint”. As defined in Lin et al. (2003), it provides the concentration change (in parts per million, ppm) at the receptor for a unit surface flux (in  $\mu\text{mol m}^{-2}\text{s}^{-1}$ ) persisting over a given time interval; its units are  $\text{ppm } \mu\text{mol}^{-1}\text{m}^2\text{s}$ . A plot of the footprints for the same 6-h time period as in Fig. 7 is shown in Fig. 8. The effect is small, but not negligible, in this case.

### 3.4 Mass conservation

As discussed in Sect. 2.5, spatial and temporal interpolations of model fields and variable transformations from the variables used in the NWP model to those used in the LPDM can lead to fields that no longer conserve mass, particularly when instantaneous wind fields are used. To diagnose the lack of mass conservation in the meteorological input fields (and apply a first-order correction), the terms in the mass continuity equation are evaluated from the available wind and density fields, and the cumulative mass violation is tallied within STILT for each particle (Lin et al. 2003). To test the degree to which mass is conserved using WRF fields, 2-day back trajectories were computed from the Argyle tower for six arbitrarily chosen times in July (08 UTC, 08 July; 15 UTC, 11 July; 22 UTC, 14 July; 05 UTC, 18 July; 12 UTC, 21 July; 19 UTC, 24 July), using 1,000 particles each. The distribution of the cumulative fractional change in mass  $d\text{mass}$  (equal to 1 for perfect mass conservation, and equal to 0.5 for a 50% loss

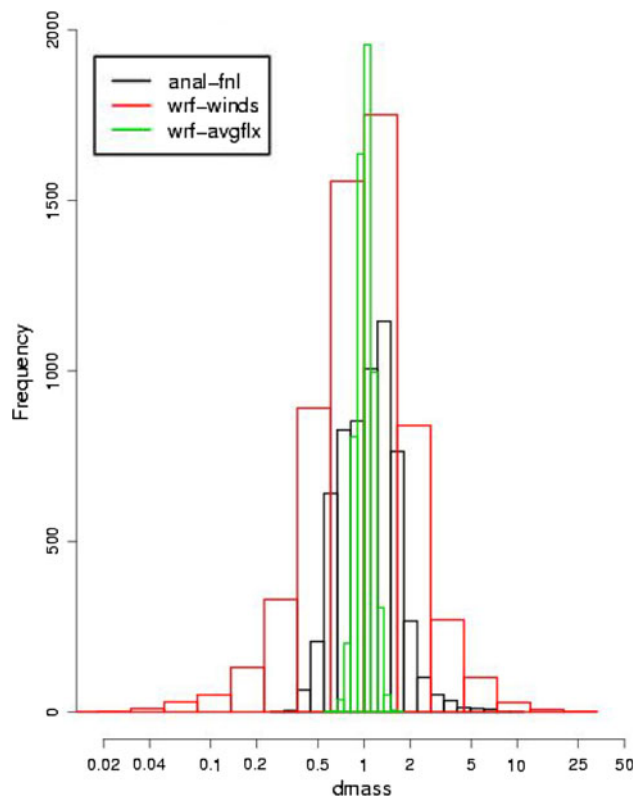


**Fig. 9** Histogram of mass conservation parameter  $d\text{mass}$  at the end of 2-day trajectories for 6 dates in July 2004, using global analysis fields (*anal-fnl*), and outer domain WRF instantaneous wind velocities (*wrf-winds*) and time-averaged fluxes (*wrf-avgflx*)

of mass) is shown in Fig. 9 for trajectories computed using the outer domain WRF fields, using either time-averaged (mass-coupled) winds or instantaneous winds, and using global NCEP analysis fields. Using time-averaged winds results in much better mass conservation properties of the interpolated wind fields, with WRF fields going from being

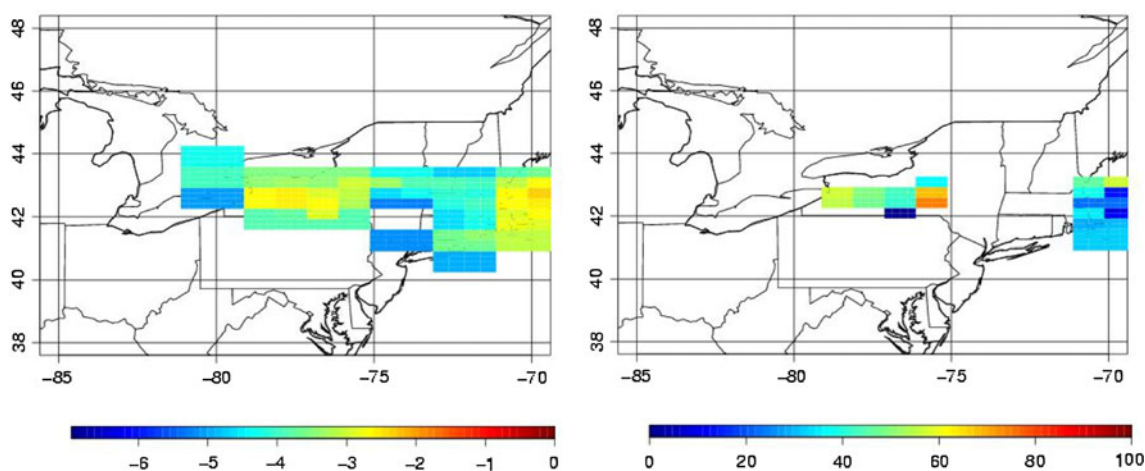


**Fig. 8** Footprints for the trajectories with convection shown in Fig. 7, plotted for values between  $10^{-7}$  and 1 using a logarithmic color scale (*left panel*). The *right panel* shows the percentage difference between convective and non-convective footprints for footprints exceeding  $10^{-3}$

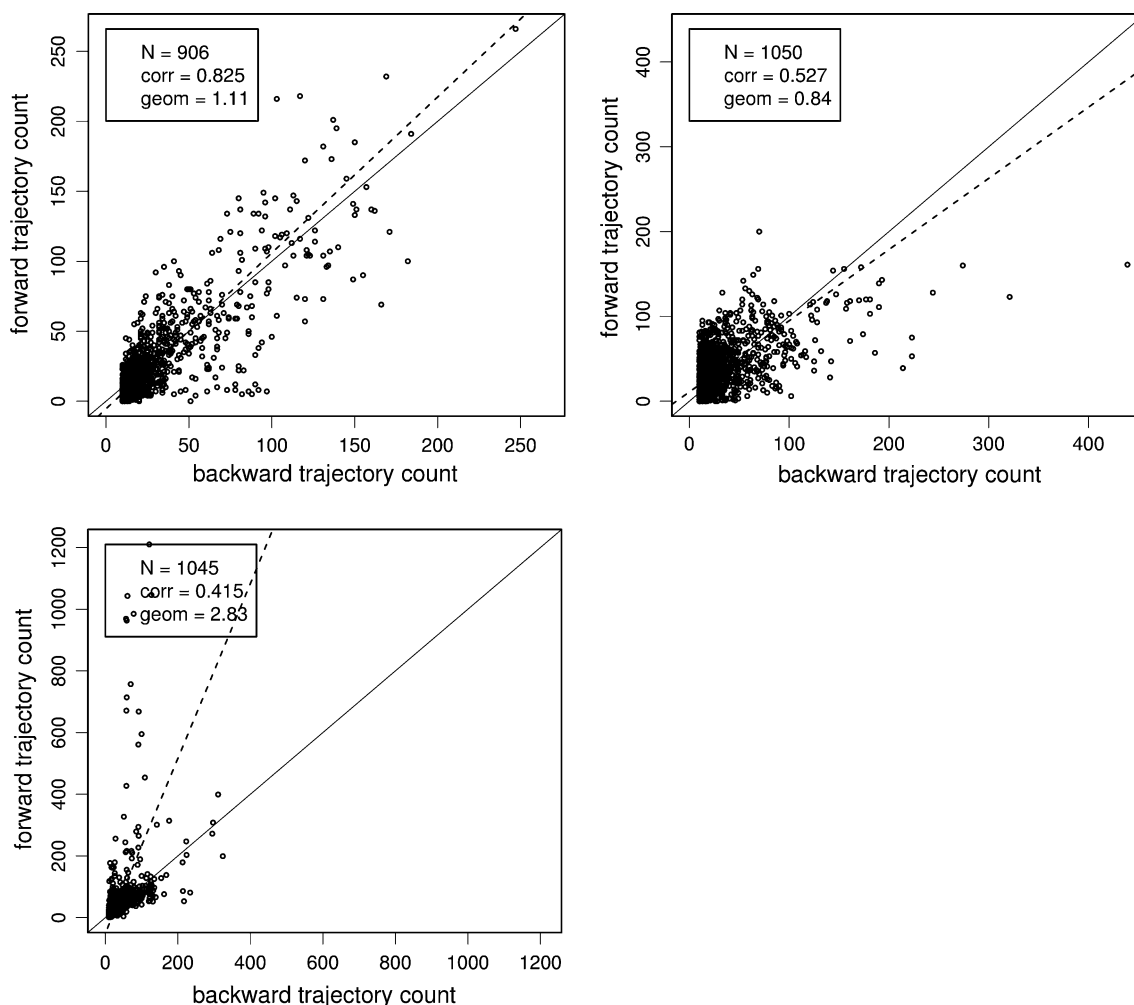


**Fig. 10** Scatterplot of forward–backward trajectory particle counts. *Top left* WRF time-averaged winds; *top right* WRF instantaneous winds, *bottom left* global analysis fields. The regression line (geometric mean of forward regressed against backward and vice

versa) is *dashed*, the 1:1 line is *solid*. *Text box* shows the number of data points in the plots, the correlation coefficient, and the slope of the geometric mean regression line

worse than the global analysis fields to being noticeably better.

By design, the *dmass* diagnostic only tests the mass conservation properties of the gridded component of the total wind field driving the trajectory calculations. A more comprehensive test of mass conservation, involving both the gridded and the stochastic components, is given by the well-mixed criterion (see Sect. 2.7.2). Violations of the well-mixed criterion cause unphysical accumulations of particles in low turbulence regions or at boundaries, leading to erroneous simulations of tracer concentrations. Our implementation of this test, based on explicit forward and backward trajectories, follows the procedure outlined by Lin et al. (2003). The backward trajectories for the six receptors used for Fig. 9 were used to define a source region for the receptor location. For each receptor, the source region was then subdivided into longitude–latitude

boxes, and an equally sized box was placed around the Argyle receptor location. Back trajectories were then computed for a total of 15,000 particles, using receptor locations randomly placed within a three-dimensional receptor box of 100-m depth centered at the Argyle tower height of 107 m above ground. For each of the previously identified source boxes (further subdivided into 100-m vertical intervals from 0 to 1 km) with a minimum of 10 particles originating from it, forward trajectories were then computed, using 15,000 particles from randomly chosen locations inside the source box. For perfect adherence to the well-mixed criterion, the number of particles found to originate from the source box in the back trajectories would be equal to the number of particles in the forward trajectories that arrive in the receptor box. A scatterplot of corresponding forward and backward trajectory particle counts is shown in Fig. 10 for the WRF outer domain

instantaneous winds and time-averaged winds. Also shown are the results for the operational NCEP global analysis fields (also referred to as “FNL”). Both sets of trajectories computed using instantaneous winds have large scatter and small correlation coefficients, with significantly better correlations for the WRF time-averaged winds (the 95% confidence intervals for the correlation coefficients are (0.36, 0.46) for the analysis trajectories, (0.48, 0.57) for the WRF winds trajectories, and (0.80, 0.84) for the WRF time-averaged winds trajectories). The slope of the regression line is also closer to the perfect slope for the WRF time-averaged winds. The regression line slopes for FNL (and, to a lesser extent, for the WRF instantaneous winds) show considerable variability when computed separately for the six receptors (the large slope and low aggregate correlation shown in Fig. 10 are largely caused by large slopes on 18 July and 21 July); however, the regression line slopes for the WRF time-averaged winds were quite consistent. These results thus confirm the conclusion reached from the analysis of the *d<sub>mass</sub>* diagnostic, that the use of time-averaged winds from WRF is crucial for mass-conserving LPDM trajectory computations.

#### 4 Summary and future work

A description of the coupled WRF–STILT Lagrangian particle mesoscale modeling system is provided, and its performance is illustrated for a carbon budget study over the North American continent. The use of (nonstandard) time-averaged, mass-coupled velocity fields from the WRF model was found to be crucial in improving the mass conservation properties of the coupled modeling system. Sensitivity to other aspects of the mesoscale model fields, such as the use of high-resolution nested domains and the inclusion of convective fluxes, was found to be highly case dependent. Since uncertainties due to transport errors can have a large impact on carbon budget computations and inferred source strengths (Gerbig et al. 2008; Gloor et al. 1999; Lin and Gerbig 2005), this suggests that a case-dependent evaluation of the sensitivities and associated uncertainties may be needed for these applications.

The WRF–STILT modeling system has been applied to a number of other applications. To support the top–down estimates of surface fluxes of CO<sub>2</sub> and other greenhouse gases from available tower and aircraft measurements of trace gas concentrations, multi-year simulations at a resolution of 10 km, and down to 2 km for selected tower locations, have been generated for the North American continent (Michalak et al. 2007; Gourdji et al. 2009) using version 2.2 of WRF with nudging to the NARR analysis. WRF–STILT has been used for estimates of methane fluxes by Kort et al. (2008) and Zhao et al. (2009), with additional

efforts underway for an expanded analysis of non-CO<sub>2</sub> greenhouse gas emissions (e.g., [http://nacp.oml.gov/mast-dc/int\\_synth\\_greenhouse.shtml](http://nacp.oml.gov/mast-dc/int_synth_greenhouse.shtml)).

Current work continues on both the WRF and STILT models. As a community model, WRF continues to evolve with added capabilities and improved parameterization packages being added continually (the customizations described here are included in release 3.2). Of particular interest to modeling of the carbon cycle are efforts to improve the radiative transfer computations. For example, Iacono et al. (2009) evaluated the effect of introducing a new radiation package into WRF version 3.1 (RRTMG, Iacono et al. 2008), and documented small but consistent improvements in the short-wave flux incident at the surface, a critical parameter for modeling the biospheric uptake of CO<sub>2</sub> by photosynthesis. Options to control error growth now include not only gridpoint nudging, but also observation and spectral nudging, and the four-dimensional variational system under development for WRF.

The STILT model has undergone a number of upgrades, most recently a merging with parts of the latest HYSPLIT code, resulting in improved handling of nested fields. The most up-to-date information on the STILT model is available at <http://www.bgc-jena.mpg.de/bgc-systems/projects/stilt/pmwiki/pmwiki.php>.

**Acknowledgments** Work at AER has been supported by the NASA Terrestrial Ecology Program (contract NNH05CC42C) and the National Science Foundation Atmospheric Chemistry Program (Grant ATM-0836153). The original manuscript was improved through constructive reviews by Arlyn Andrews (NOAA/Earth System Research Laboratory) and an anonymous reviewer.

#### References

- Arakawa A, Lamb V (1977) Computational design of the basic dynamical processes of the UCLA general circulation model. In: Methods in computational physics, vol 17. Academic Press, pp 174–267
- Avey L, Garrett TJ, Stohl A (2007) Evaluation of the aerosol indirect effect using satellite, tracer transport model, and aircraft data from the International Consortium for Atmospheric Research on Transport and Transformation. *J Geophys Res* 112:D10S33. doi: 10.1029/2006JD007581
- Buckley RL (2000) Modeling atmospheric deposition from a cesium release in Spain using a stochastic transport model, 11th Joint Conference on the Applications of Air Pollution Meteorology with the Air and Waste Management Association, Long Beach, CA, American Meteorological Society, pp 190–195
- Calvin W et al (2007) Report from the 2013 Mars Science Orbiter (MSO) Second Science Group, 72 pp., posted June 2007 by the Mars Exploration Program Analysis Group (MEPAG). Available at <http://mepag.jpl.nasa.gov/reports/index.html>
- Chen S-H, Sun W-Y (2002) A one-dimensional time dependent cloud model. *J Meteorol Soc Jpn* 80(1):99–118
- Chou M-D, Suarez M (1994) An efficient thermal infrared radiation parameterization for use in general circulation models. Tech Memo 104606, NASA, Washington, DC

- Cotton WR et al (2003) RAMS 2001: current status and future directions. *Meteorol Atmos Phys* 82:5–29
- Draxler RR, Hess GD (1997) Description of the HYSPLIT\_4 modeling system, NOAA Tech. Memo. ERL ARL-224, 24 pp
- Draxler RR, Hess GD (1998) An overview of the HYSPLIT\_4 modeling system for trajectories, dispersion, and deposition. *Aust Meteorol Mag* 47:295–308
- Fast JD (2005) Evaluation of the boundary layer characteristics and particulates in Mexico City predicted by WRF. In: Joint WRF/MM5 Users' Workshop, NCAR, Boulder, CO. Available from <http://www.wrf-model.org/wrfadmin/presentations.php>
- Flesch TK, Wilson JE, Yee E (1995) Backward-time Lagrangian stochastic dispersion models and their application to estimate gaseous emissions. *J Appl Meteorol* 34:1320–1332
- Forster C et al (2004) Lagrangian transport model forecasts and a transport climatology for the Intercontinental Transport and Chemical Transformation 2002 (ITCT 2K2) measurement campaign. *J Geophys Res* 109:D07S92. doi:10.1029/2003JD003589
- Forster C, Stohl A, Seibert P (2007) Parameterization of convective transport in a Lagrangian particle dispersion model and its evaluation. *J Appl Meteorol Clim* 46:403–422
- Freitas SR, Silva Dias MAF, Silva Dias PL, Longo KM, Artaxo P, Andreae MO, Fisher H (2000) A convective kinematic trajectory technique for low-resolution atmospheric models. *J Geophys Res* 105(D19):24,375–24386
- Freitas SR, Longo KM, Silva Dias MAF, Silva Dias PL, Chatfield R, Prins E, Artaxo P, Grell G, Recuero FS (2005) Monitoring transport of biomass burning emissions in South America. *Environ Fluid Mech* 5:135–167
- Freitas SR, Longo KM, Silva Dias MAF, Chatfield R, Silva Dias P, Artaxo P, Andreae MO, Grell G, Rodrigues LF, Fazenda A, Panetta J (2009) The coupled aerosol and tracer transport model to the Brazilian developments on the Regional Atmospheric Modeling System (CATT-BRAMS)—Part 1: model description and evaluation. *Atmos Chem Phys* 9:2843–2861
- Galmarini S, Bianconi R, Klug W, Mikkelsen T, Addis R, Andronopoulos S, Astrup P, Baklanov A, Bartniki J, Bartzis JC, Bellasio R, Bompay F, Buckley R, Bouzom M, Champion H, D'Amours R, Davakis E, Eleveld H, Geertsema GT, Glaab H, Kollax M, Ilvonen M, Manning A, Pechinger U, Persson C, Polreich E, Potemski S, Prodanova M, Saltbones J, Slaper H, Sofiev MA, Syrakov D, Sørensen JH, Van der Auwera L, Valkama I, Zelazny R (2004) Ensemble dispersion forecasting—Part I: concept, approach and indicators. *Atmos Environ* 38:4607–4617
- Gerbig C, Lin JC, Wofsy SC, Daube BC, Andrews AE, Stephens BB, Bakwin PS, Grainger CA (2003) Towards constraining regional scale fluxes of CO<sub>2</sub> with atmospheric observations over a continent: 2. Analysis of COBRA data using a receptor-oriented framework. *J Geophys Res* 108(D24):4757. doi:10.1029/2003JD003770
- Gerbig C, Korner S, Lin JC (2008) Vertical mixing in atmospheric tracer transport models: error characterization and propagation. *Atmos Chem Phys* 8:591–602
- Gloor M, Fan S-M, Pacala S, Sarmiento J, Ramonet M (1999) A model-based evaluation of inversions of atmospheric transport, using annual mean mixing ratios, as a tool to monitor fluxes of nonreactive trace substances like CO<sub>2</sub> on a continental scale. *J Geophys Res* 104(D12):14245–14260
- Gourdji SM, Hirsch AI, Mueller KL, Andrews AE, Michalak AM (2009) Regional-scale geostatistical inverse modeling of North American CO<sub>2</sub> fluxes: a synthetic data study. *Atmos Chem Phys Discuss* 9:22407–22458
- Grell G (1993) Prognostic evaluation of assumptions used by cumulus parameterizations. *Mon Weather Rev* 121:764–787
- Grell GA, Devenyi D (2002) A generalized approach to parameterizing convection combining ensemble and data assimilation techniques. *Geophys Res Lett* 29:1693. doi:10.1029/2002GL015311
- Grell GA, Dudhia J, Stauffer DR (1994) A description of the fifth generation Penn State/NCAR mesoscale model (MM5). *NCAR/Tech. Note-398 + STR*, pp. 64–72, Natl Cent For Atmos Res, Boulder, CO
- Iacono MJ, Delamere JS, Mlawer EJ, Shephard MW, Clough SA, Collins WD (2008) Radiative forcing by long-lived greenhouse gases: calculations with the AER radiative transfer models. *J Geophys Res* 113:D13103. doi:10.1029/2008JD009944
- Iacono MJ, Nehr Korn T, Dudhia J, Wang W (2009) Application of RRTMG/McICA to the Advanced Research WRF weather forecast model. In: Proceedings, 19th ARM science team meeting, Office of Science, US Department of Energy, Louisville, KY. Available from <http://www.arm.gov/publications/proceedings/conf19/display.php?id=NTky>
- Kort EA, Eluszkiewicz J, Stephens BB, Miller JB, Gerbig C, Nehr Korn T, Daube BC, Kaplan JO, Houweling S, Wofsy SC (2008) Emissions of CH<sub>4</sub> and N<sub>2</sub>O over the United States and Canada based on a receptor-oriented modeling framework and COBRA-NA atmospheric observations. *Geophys Res Lett* 35:L18 808. doi:10.1029/2008GL034031
- Lin JC, Gerbig C (2005) Accounting for the effect of transport errors on tracers inversions. *Geophys Res Lett* 32:L01802. doi:10.1029/2004GL021127
- Lin Y-L, Farley RD, Orville HD (1983) Bulk parameterization of the snow field in a cloud model. *J Appl Meteorol* 22(6):1065–1092
- Lin JC, Gerbig C, Wofsy SC, Daube BC, Andrews AE, Davis KJ, Grainger CA (2003) A near-field tool for simulating the upstream influence of atmospheric observations: the stochastic time-inverted lagrangian transport (STILT) model. *J Geophys Res* 108(D16):4493. doi:10.1029/2002JD003161
- Lin JC, Gerbig C, Wofsy SC, Draxler R, Chow VY, Gottlieb EW (2007) Designing Lagrangian experiments to measure regional-scale trace gas fluxes. *J Geophys Res* 112 (D13312). doi:10.1029/2006JD008077
- Medvigy D, Moorcroft PR, Avissar R, Walko RL (2005) Mass conservation and atmospheric dynamics in the regional atmospheric modeling system (RAMS). *Environ Fluid Mech* 5:109–134
- Mesinger F, DiMego G, Kalnay E, Mitchell K, Shafran PC, Ebisuzaki W, Jovic D, Woollen J, Rogers E, Berbery EH, Ek MB, Fan Y, Grumbine R, Higgins W, Li H, Lin Y, Manikin G, Parrish D, Shi W (2006) North American regional reanalysis. *Bull Am Meteorol Soc* 87(3):343–360
- Michalak AM, Mueller K, Gourdji S, Hirsch AI, Andrews AE, Lin JC, Nehr Korn T (2007) Bridging across spatial and temporal scales in North American carbon dioxide flux estimation through geostatistical analysis of scale-dependent relationships between carbon flux and auxiliary environmental data. *EOS, Trans Amer Geophys Union* 88(52), Fall Meet. Suppl., Abstract B42C-01
- Mlawer EJ, Taubman SJ, Brown PD, Iacono MJ, Clough SA (1997) Radiative transfer for inhomogeneous atmospheres: RRTM, a validated correlated-k model for the longwave. *J Geophys Res* 102(D14):16 663–16 682
- Pielke RA, McNider RT, Segal M, Mahrer Y (1983) The use of a mesoscale numerical model for evaluations of pollutant transport and diffusion in coastal regions and over irregular terrain. *Bull Am Meteor Soc* 64(3):243–249
- Pielke RA et al (1992) A comprehensive meteorological modeling system—RAMS. *Meteorol Atmos Phys* 49:69–91
- Rodean HC (1996) Stochastic Lagrangian models of turbulent diffusion. *Meteorological monographs*. American Meteorological Society, Boston, MA, 26(48):84

- Seibert P, Frank A (2004) Source-receptor matrix calculation with a Lagrangian particle dispersion model in backward mode. *Atmos Chem Phys* 4:51–63
- Skamarock WC, Klemp JB (2008) A time-split nonhydrostatic atmospheric model for weather research and forecasting applications. *J Comp Phys* 227:3465–3485
- Skamarock WC, Klemp JB, Dudhia J, Gill DO, Barker DM, Wang W, Powers JG (2005) A description of the advanced research WRF version 2. Technical Note 468 + STR, MMM Division, NCAR, Boulder, CO, 88 pp. Available from [http://www.mmm.ucar.edu/wrf/users/docs/arw\\_v2.pdf](http://www.mmm.ucar.edu/wrf/users/docs/arw_v2.pdf)
- Stohl A, Forster C, Frank A, Seibert P, Wotawa G (2005) Technical note: the Lagrangian particle dispersion model FLEXPART version 6.2. *Atmos Chem Phys* 5:2461–2474
- Thomson DJ (1987) Criteria for the selection of stochastic models of particle trajectories in turbulent flows. *J Fluid Mech* 180:529–556
- UCAR (2000) [http://www.meted.ucar.edu/nwp/9cu1/ic2/frameset.htm?opentopic\(2\)](http://www.meted.ucar.edu/nwp/9cu1/ic2/frameset.htm?opentopic(2)) Vertical Coordinates
- Uliasz M (1993) The atmospheric mesoscale dispersion modeling system (MDMS). *J Appl Meteor* 32:139–149
- Worden HM, Logan JA, Worden JR, Beer R, Bowman K, Clough SA, Eldering A, Fisher BM, Gunson MR, Herman RL, Kulawik SS, Lampel MC, Luo M, Megretskaja IA, Osterman GB, Shephard MW (2007) Comparisons of tropospheric emission spectrometer (TES) ozone profiles to ozonesondes: methods and initial results. *J Geophys Res* 112:D03309. doi:10.1029/2006JD007258
- Yamada T, Bunker S (1988) Development of a nested grid, second moment turbulence closure model and application to the 1982 ASCOT Brush Creek data simulation. *J Appl Meteor* 27(5):562–578
- Zhao C, Andrews AE, Bianco L, Eluszkiewicz J, Hirsch A, MacDonald C, Nehr Korn T, Fischer ML (2009) Atmospheric inverse estimates of methane emissions from Central California. *J Geophys Res* 114:D16302. doi:10.1029/2008JD011671